Bulletin of the Seismological Society of America, Vol. 80, No. 5, pp. 1162–1179, October 1990

BROADBAND MODELING OF LOCAL EARTHQUAKES

By Douglas S. Dreger and Donald V. Helmberger

Abstract

Three-component broadband waveforms of two small earthquakes near Upland, California, recorded on the Pasadena broadband, high dynamic range instrument, were modeled to obtain useful Green's functions for this path and to examine the sensitivity of the synthetic seismograms to perturbations of the crustal model. We assumed that the source of each event was both simple and known, as determined from the Caltech-USGS array first motions. A trapezoidal time function was chosen to fit the width of the direct *S* wave. Generalized rays, reflectivity, and finite-difference techniques were used to compute the synthetic seismograms.

We found that a simple layer over a half-space model is an adequate approximation of the upper crust along this profile. In particular, the waveforms are controlled by a relatively slow, 4-km-thick surficial layer (α = 4.5km-s^{-1}, β = 2.6 km-s^{-1}) over a faster layer (α = 5.9 km-s^{-1}, β = 3.5 km-s^{-1}). The relative amplitudes of direct and multiple S indicate that the main shock occurred at a depth of 6 km, while the aftershock occurred at a depth of 8 to 9 km. Sensitivity analyses indicate that for distances less than 50 km and for periods longer than 1 sec, the synthetic seismograms are not very sensitive to perturbations of the deep crustal structure. Analysis of upper crustal model perturbations revealed that the surficial layer is between 3 to 5 km thick. In addition, the contact between this layer and the underlying material can be smoothed with a 2-km-wide velocity gradient without adversely affecting the fit to the data. Two-dimensional finite-difference calculations show that a ridge structure beneath the recorder acts as a lowpass filter (the lower frequency phases are largely unaffected). Other two-dimensional models with ridges between the source and receiver clearly did not fit the data. Synthetic seismograms computed for the best fitting model were used to estimate a long-period moment of (6 ± 2) × 10^{22} dyne-cm (M_L = 4.6) and 1 × 10^{22} dyne-cm (M_L = 3.7) with identical triangular source-time durations of 0.3 sec. Assuming the same fault dimension of 0.4 km from standard scaling laws, stress drop estimates of 410 and 70 bars are obtained for the two events, respectively. Generally, we found that it is possible to reproduce local waveforms at frequencies up to 1 Hz without a complete knowledge of fine structural detail. Resulting Green's functions can be useful in studying historic events, and in simulations of large events from a given source region.

Introduction

The installation of the Pasadena, California, (PAS) very broadband, high dynamic range instrument (Wielandt-Streckeisen sensor and Quanterra data logger) of the IRIS (International Research Institution for Seismology) and TERRAscope networks has allowed the comparison of seismic waveforms from events over a wide range of magnitudes. On traditional instruments, however, such as the short-period Wood-Anderson (WASP) and the long-period Wood-Anderson (WALP), there is a rather narrow range of earthquake magnitudes that provide on-scale waveforms at a given receiver distance. In many cases, local events in the range of M_L = 3.0 to about M_L = 5.0 from a common source region have been observed to have similar waveforms. Figure 1 shows the location of the PAS station and four local earthquakes. Figure 2 shows an example of two small local earthquakes that occurred

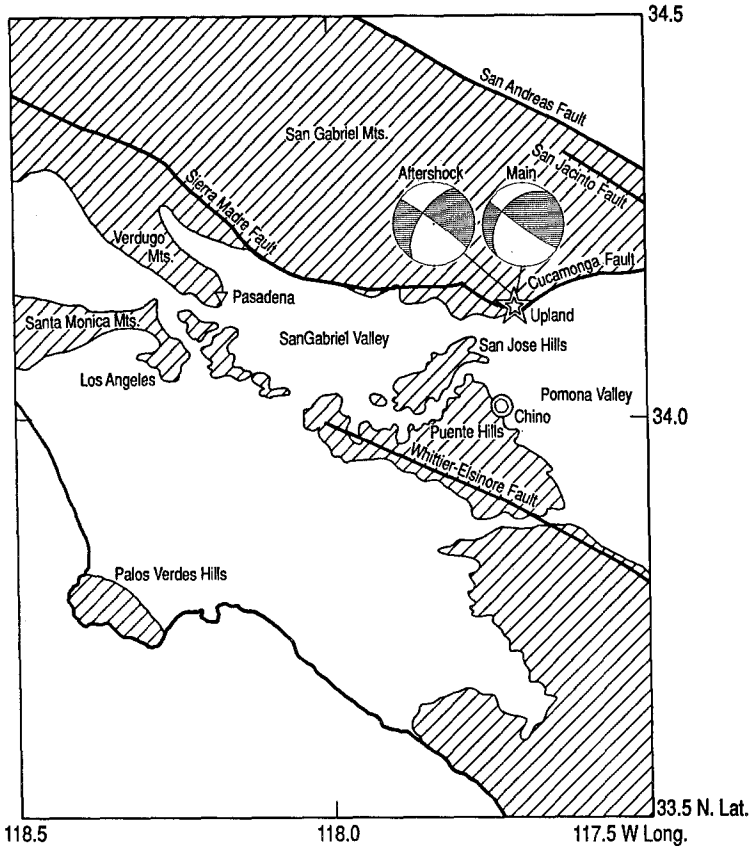

FIG. 1. Location map: the inverted triangle is the Pasadena station, the circles mark the Chino events, and the stars denote the Upland events. Focal mechanisms for the two Upland earthquakes determined from USGS/Caltech seismic array first-motion polarities are also given. Hatched regions represent areas of shallow or surficial basement rocks after Yerkes *et al.* (1965).

near Chino, California, in February 1989. These tangential component records were recorded on the very broadband channel of the PAS instrument, integrated, and then convolved with the instrument response of a WASP instrument. The amplitudes given on this figure are the peak amplitudes of the WASP instrument in centimeters. Although different in size by more than an order of magnitude, these two events have nearly identical seismograms, demonstrating the deterministic nature of the records. It is evident that the smaller event would be barely recognizable on a natural WASP record, while an event slightly larger than the larger of the two would be off-scale.

Events in this region are well located since they occurred within the dense USGS-Caltech array. In addition, focal mechanisms from first motions are easily obtained and appear quite accurate for events in this magnitude range. These smaller events also have simpler sources than larger events and generally do not show the complexity associated with rupture on finite distributed faults with or without asperities. Furthermore, there are more earthquakes in this size range than larger earthquakes increasing the data set.

In short, we can assume the events are well located point sources and analyze these seismograms in terms of propagational effects to study the crustal structure.

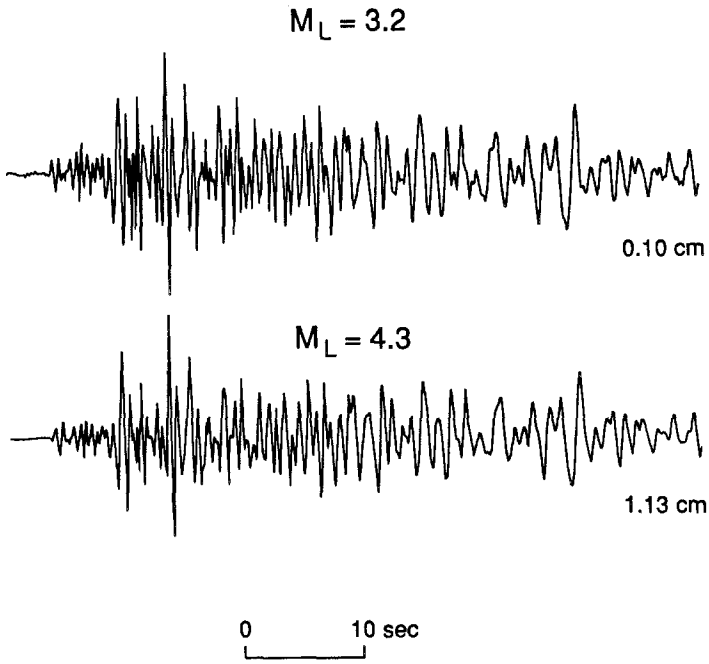

FIG. 2. Tangential components of the 16 February 1988 (M_L = 3.2) and 18 February 1988 (M_L = 4.3) Chino earthquakes. The integrated broadband recordings have been convolved with a short-period Wood-Anderson instrument response. Each seismogram is scaled to its maximum amplitude.

The purpose of this paper is to demonstrate the methodology of obtaining accurate Green's functions from broadband data. We also intend to show that a large quantity of information about earthquake sources and propagation effects can be extracted from the broadband waveform data recorded at a single station. This study has two parts. First, a crustal model is determined and the modeling approach is discussed. Second, the sensitivity of the synthetic seismograms with respect to two-dimensional model perturbations is examined. Once the crustal structure or Green's functions are known, they can be used to study the sources of sparsely recorded historic earthquakes or to scale up the source and estimate strong ground motion for larger earthquakes (Woods *et al.*, 1990).

DATA AND PROCESSING

The data were recorded at the IRIS-TERRAscope instrument, PAS. The gain of this instrument is constant in ground velocity between 0.0027 and 7 Hz for the very broadband channel. Integration within this frequency band produces displacement seismograms that can be convolved with the response of any instrument to obtain equivalent instrument seismograms. In this study, the displacement seismograms, as well as the WASP and WALP instrument seismograms, are used in the forward modeling approach.

Two small earthquakes (M_L = 4.6 and 3.7) were recorded by this instrument on 26 June 1988 and 6 July 1988, respectively. Both of these earthquakes occurred in the Upland, California area (Fig. 1), and the hypocenters located by the Southern California Network are within 1 km of each other, at a depth of about 8 to 9 km. These events occurred at a distance of about 43 km and the azimuth to the PAS station is 272°. Two focal mechanisms were obtained from first-motion polarities

on the Southern California array. They are $\phi = 221°$, $\delta = 40°$, $\lambda = 8°$, for the main shock, and $\phi = 212°$, $\delta = 60°$, $\lambda = -6°$ for the aftershock (L. Jones, personal comm.). Figure 1 shows that these mechanisms are very similar with a slight difference in the dip angle. Figure 3 displays the three-component displacement records and the WASP instrument seismograms. It is evident that these two earthquakes have very similar waveforms, however the similarity is not as great as for the earthquakes presented in Figure 2. Since the events occurred in nearly the same location, the differences in the waveforms are probably due to differing source history, orientation, and/or location. The most significant difference in the waveforms for the two events is in the relative amplitudes of the various S-wave phases on the tangential components. The identification of these phases and an understanding of the differences of the waveforms is a priority in modeling these events to obtain useful Green's functions.

Methodology

The approach taken in this study was to identify the phases in the waveforms via forward modeling using generalized ray theory (GRT). See Helmberger (1974, 1983)

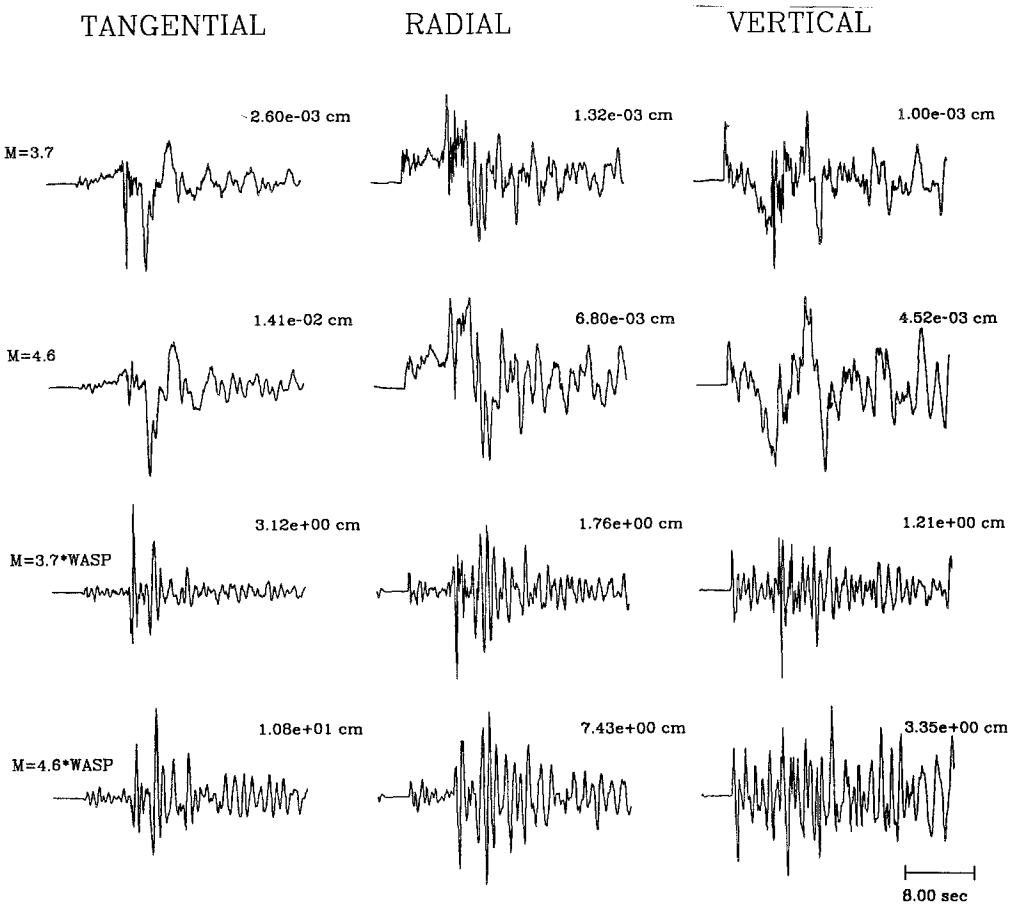

FIG. 3. Three component displacement and short-period Wood-Anderson data for the 26 June 1988 (M_L = 4.6) and 6 July 1988 (M_L = 3.7) Upland events. Each seismogram is scaled to its maximum amplitude.

for details. GRT is especially useful for this purpose because it allows one to build the waveform with individual rays. Since both source and propagation parameters are needed in computing synthetic seismograms, the source parameters must be constrained by other seismic measurements or assumptions in order to study crustal structure. Here we hold the source parameters (location, focal mechanism) determined from first-motion studies utilizing the entire Caltech-USGS network data fixed. We assumed a point source for both events, with a trapezoidal source-time function. A 0.15-sec rise time, 0.15-sec duration, and 0.15-sec fall time was determined by modeling the width of the direct S wave. The same source-time function was used for both the main shock and the aftershock. In modeling the tangential components, we found that the two focal mechanisms produced very similar synthetics. With the exception of Figure 9, all of the synthetic seismograms presented in this paper were constructed using the focal mechanism of the main shock. In Figure 9, we compare synthetics constructed for both focal mechanisms. With the source parameters constrained, the velocity model was perturbed until good agreement with the data was obtained.

Modeling Results

The tangential component seismograms for both events contain a large amplitude phase which arrives after the initial direct S wave. This phase is identified as a near receiver multiple within a near surface layer. In addition, there is a long-period phase arriving after the multiple which is interpreted as a Love wave. A simple layer over a half-space model works well in explaining the occurrence of these phases in the data. Figure 4 shows how the synthetics are developed with the

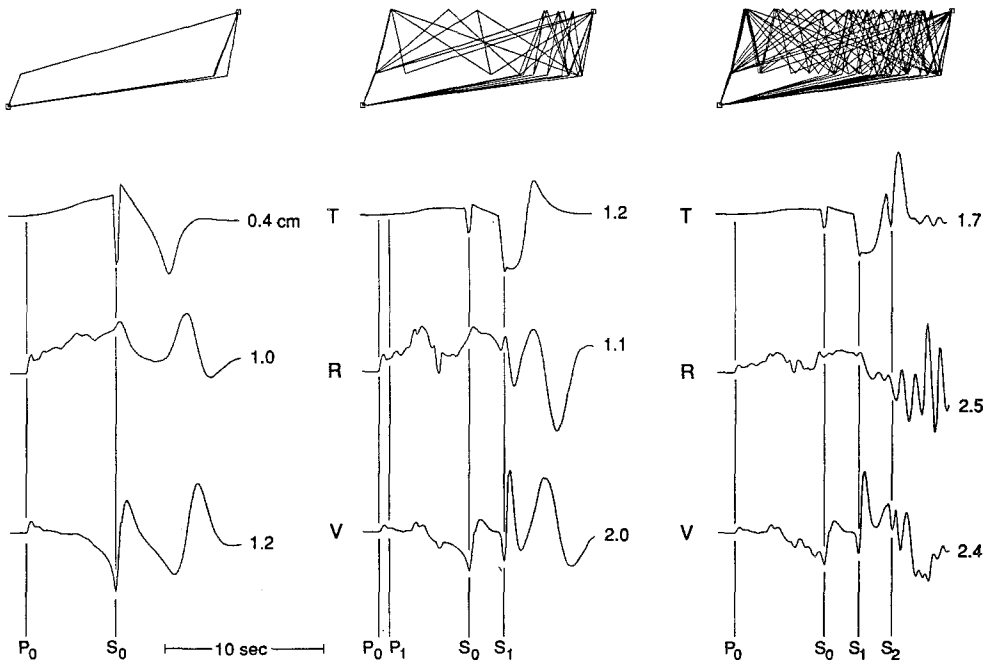

FIG. 4. The addition of rays to construct synthetic displacement waveforms for the tangential (T), radial (R), and vertical (V) components. A moment of 10^{25} dyne-cm was used. S_0 and P_0 are the direct S and P waves, respectively. Note the ramp like near field term on the tangential component. Each seismogram is scaled to its maximum amplitude.

addition of rays, aiding the identification of the multiple phases (S_1 and S_2). The first two layers of the velocity model LOHS1 (Table 1) were used in computing these synthetics. The phases S_0, S_1, S_2 are all observed in the data, especially on the tangential records. The ramp-like feature beginning at the P-wave travel time and continuing to the arrival of the direct S wave (S_0) arises with the addition of near-field terms in the calculations and is evident on the tangential component displacement records (Fig. 3). The traditional WASP and WALP instruments filter the near-field phase from the data (Fig. 5). This model also produces the longer-period Love wave which arrives after S_1. Five phases have been identified on the tangential component seismograms using GRT. It is rather surprising that such a simple model can give rise to such complexity. Figure 5 compares the tangential component GRT synthetic seismograms for the preferred model LOHS1, to the Upland data. The amplitudes in this figure are the maximum amplitudes in centimeters. The amplitudes of the displacement synthetics were scaled to the amplitudes

TABLE 1

ONE DIMENSIONAL VELOCITY MODELS

LOHS1				SoCal				LOHS2				L1				L2			
V_p	V_s	ρ	Z	V_p	V_s	ρ	Z	V_p	V_s	ρ	Z	V_p	V_s	ρ	Z	V_p	V_s	ρ	Z
4.5	2.6	2.4	0.0	5.5	3.18	2.4	0.0	4.7	2.4	2.4	0.0	4.5	2.6	2.4	0.0	4.5	2.6	2.4	0.0
5.9	3.5	2.67	4.0	6.3	3.64	2.67	5.5	5.5	3.5	2.67	3.3	5.9	3.5	2.67	4.0	5.9	3.5	2.67	4.0
6.6	3.8	2.8	16.0	6.7	3.87	2.8	16.0	6.0	3.6	2.7	10.3	6.5	3.75	2.7	10.0	6.5	3.75	2.7	10.0
8.0	4.1	3.1	26.0	7.8	4.5	3.0	37.0	6.6	3.81	2.8	22.3	5.6	3.23	2.7	15.0	6.55	3.78	2.8	15.0
8.2	4.2	3.3	30.0					7.4	4.27	2.95	26.3	6.6	3.81	2.8	21.0	6.6	3.81	2.8	21.0
								8.0	4.4	3.0	30.3	7.2	4.16	2.9	23.0	7.2	4.16	2.9	23.0
												7.4	4.27	2.95	25.0	7.4	4.27	2.95	25.0
												7.6	4.39	3.0	27.0	7.6	4.39	3.0	27.0
												8.0	4.62	3.2	32.0	8.0	4.62	3.2	32.0
												8.3	4.8	3.35	38.0	8.3	4.8	3.35	38.0

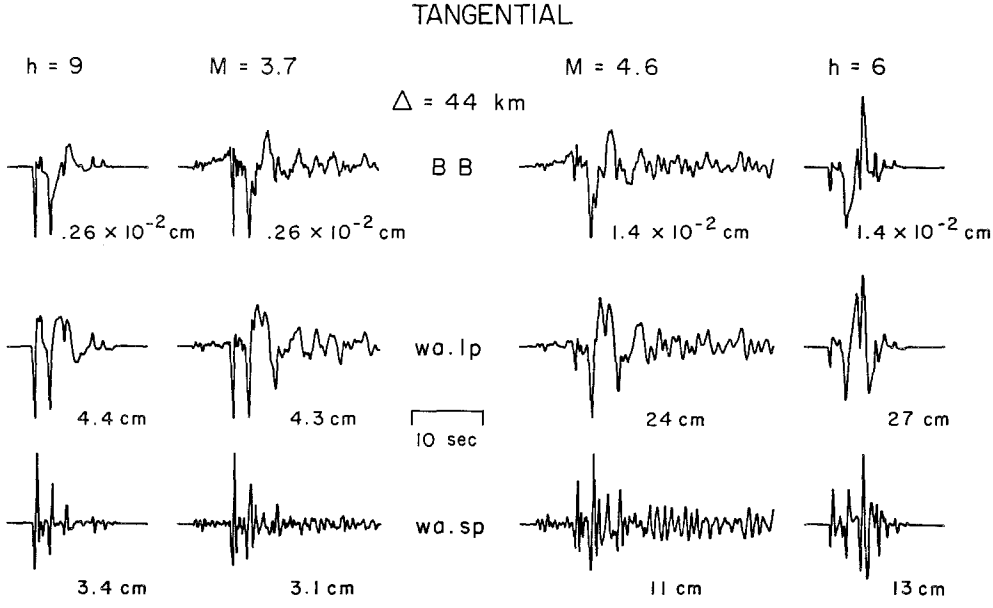

FIG. 5. Comparison of tangential component synthetic seismograms with data (synthetics were computed with generalized rays). Moments are 1.7×10^{22} and 7.9×10^{22} dyne-cm for the aftershock and main shock, respectively. Each seismogram is scaled to its maximum amplitude. Source depths of 6 km and 9 km were used for the main shock and the aftershock synthetics, respectively.

of the displacement data by multiplying by a moment. The same moment was used for the WASP and WALP synthetics, and there is good agreement in absolute amplitudes in the frequency bands of these instruments. The fits of the synthetics to the tangential data are exceptional. The S_0, S_1, and Love waves are all well modeled. In these calculations the near-field problem was neglected. The addition of the near-field terms in the calculation would serve to improve the fits of the synthetics to the data by including the ramp-like phase arriving between the direct P and S phases. In addition, it was found that the amplitude ratio of S_0 and S_1 on the tangential component record of the main shock is better modeled with a source depth of 6 km. The effect of differing source depth on the synthetics is discussed later.

Figures 6 and 7 compare the radial and vertical component synthetics, respectively, with the data. These synthetics were computed using a reflectivity code vecorized and programmed by S. Mallick and M. Sen. This method also neglects the near-field problem. These synthetics were also computed for the LOHS1 (Table 1) velocity model. The maximum amplitudes in centimeters are given, and as in Figure 5 the amplitude of the displacement synthetics were scaled to the data by multiplying by the appropriate moment. The same moment was then used for the WASP and WALP synthetics. The fit of the radial and vertical synthetics to the data is not as good as for the tangential component, however, at longer periods model LOHS1 works well. As in Figure 5, there is also good agreement in the maximum amplitudes of the synthetics and the data convolved with the WASP and WALP instruments. The coupled P-SV system is more sensitive to lateral heterogeneity, hence our simple model does not explain the high frequencies (WASP) very well; however the fits to the WALP instrument and the displacement data are good. One of the problems with the fit to the radial and vertical components, is that the relative amplitude of the direct P wave is not well modeled for the 6-km source

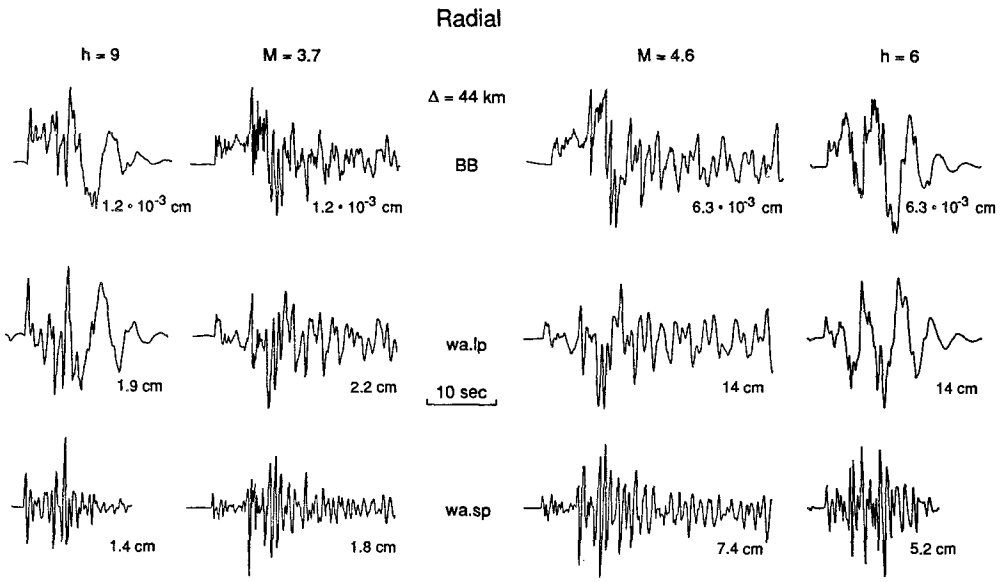

FIG. 6. Comparison of radial component synthetic seismograms with data (synthetics were computed with reflectivity). Moments are 1.5×10^{22} and 8.2×10^{22} dyne-cm for the aftershock and the main shock, respectively. Each seismogram is scaled to its maximum amplitude. Source depths of 6 km and 9 km were used for the main shock and the aftershock synthetics, respectively.

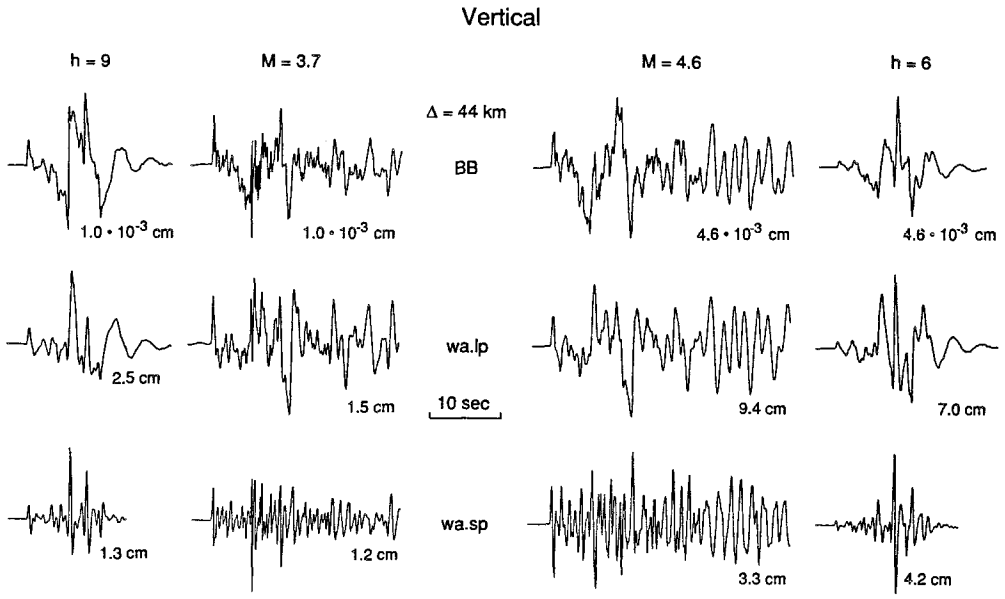

FIG. 7. Comparison of vertical component synthetic seismograms with data (synthetics were computed with reflectivity). Moments are 7.7×10^{21} and 1.9×10^{22} dyne-cm for the aftershock and the main shock, respectively. Each seismogram is scaled to its maximum amplitude. Source depths of 6 km and 9 km were used for the main shock and the aftershock synthetics, respectively.

depth. This is especially true for the vertical component. The relative strength of the direct P wave (P_0) is nearly the same for both events, yet the synthetics show large differences in relative amplitude. In addition, the vertical component waveform of the main shock is better fit by the synthetic for a 9-km source depth. There is some indication that the disagreement of the synthetics to the radial and vertical component data is in part due to our choice of source mechanism, and this is discussed later. The later arriving coda is difficult to model, but the amplitude does show a strong depth dependence. We plan to address this subject in a future study. It is important to note that, although the model used contains deeper structure, the tangential and the long-period radial and vertical component waveforms are really controlled by a layer over a half-space, composed of the velocities of the top two layers of the model LOHS1.

Figure 8 shows synthetics for different source depths (3 to 17 km) constructed with the LOHS1 model, and the main-shock focal mechanism. These displacement synthetics were computed with the reflectivity code discussed earlier. Direct S (S_0) increases in amplitude with increasing depth, while multiple S (S_1) becomes more nodal and the strength of the Love wave and Rayleigh wave decreases. The character of the synthetic waveforms become simpler with greater depth for all three components. The synthetics at 3-km depth are considerably different in waveform and amplitude. The large amplitudes are due to short-period energy trapped within the near surface layer. The longer-period first arrival is a headwave. Figures 9a and 9b also show synthetics for source depths between 6 km and 9 km, for the main-shock and the aftershock focal mechanisms, respectively. This figure demonstrates that the two focal mechanisms produce similar waveforms on the tangential component. The relative amplitudes of S_0 and S_1 are not due to the differences in the focal mechanisms. In addition, we perturbed the focal mechanism and found that, when direct S (S_0) became nodal, a reflection from the layer at 16 km depth arriving just

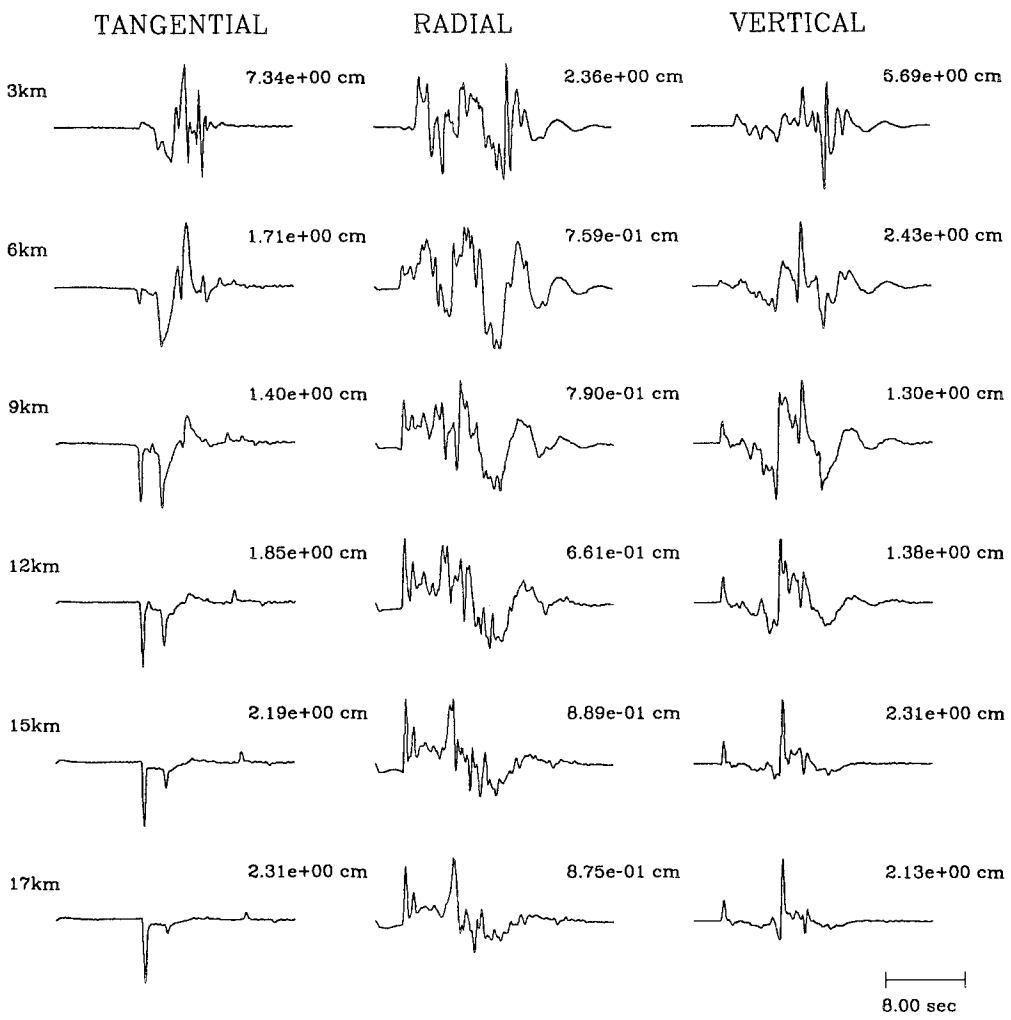

FIG. 8. Profile of synthetic seismograms for source depths from 3 to 17 km. The synthetics were constructed with the main-shock focal mechanism and a moment of 10^{25} dyne-cm. Each seismogram is scaled to its maximum amplitude.

after S_0 became large compared to either S_0 or S_1, and the overall waveform was drastically changed. Judging from Figure 9a, the tangential component of the main shock is best modeled with a 6-km source depth, and the aftershock is best modeled with a 9-km source depth. Figure 9b shows the source depth sensitivity of the synthetics for the aftershock focal mechanism. Again, the tangential component of the main shock is best modeled with a source depth of 6 km and the aftershock between 8 km and 9 km. Use of the aftershock mechanism improves the fit to the radial and vertical components, however. The relative amplitude of direct P is more consistent for the different depths than it was when the main-shock focal mechanism was used. Moreover, there is less change of the vertical synthetic waveforms with increasing source depth. The near-field effect on the tangential component synthetics has already been discussed, but there is also a near-field effect on the radial and vertical components expressed as drift between P_0 and S_0 (Helmberger and Vidale, 1988). Comparing the synthetics in Figures 6 and 4, one can see that in fact the radial component does increase in maximum amplitude and that the large

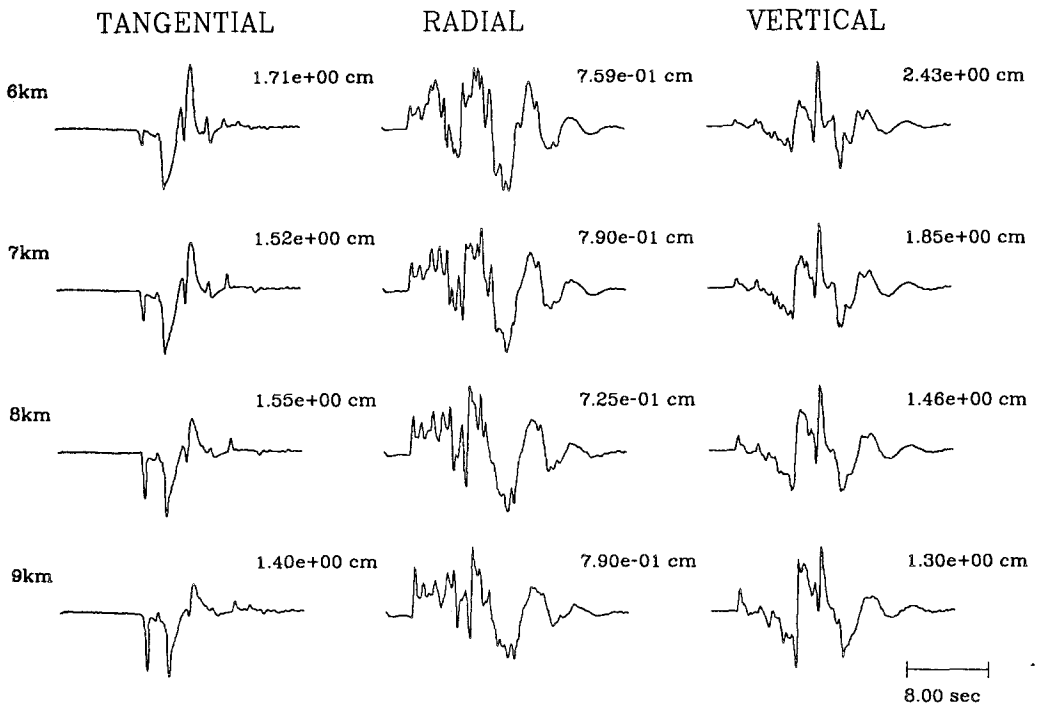

(a)

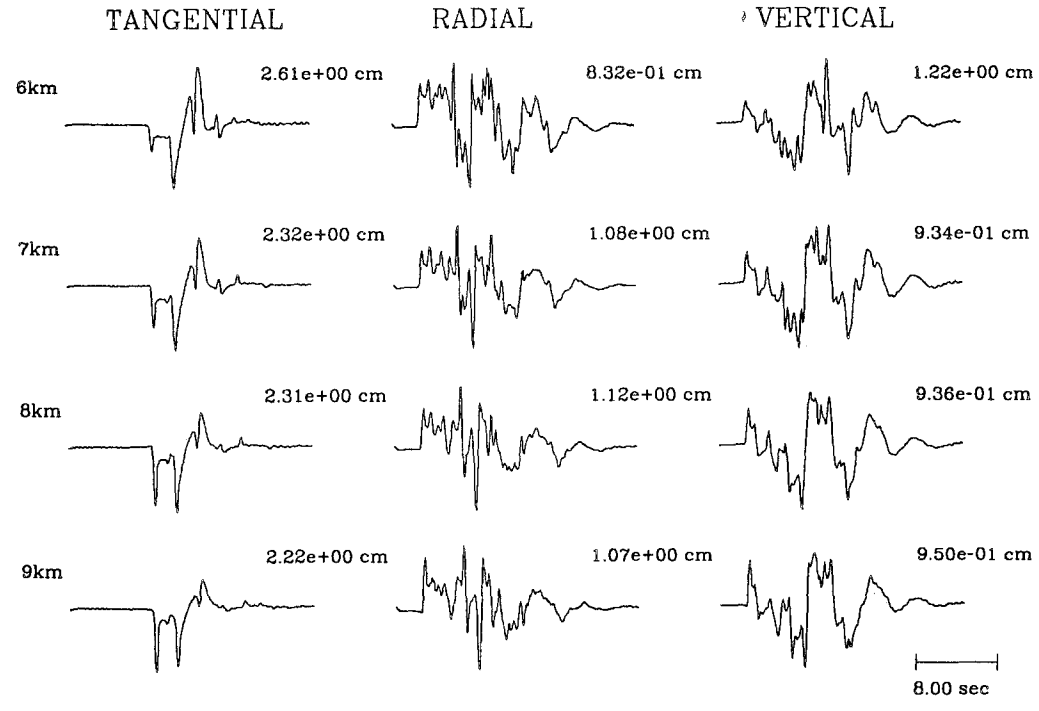

(b)

FIG. 9. Profile of synthetic seismograms for source depths from 6 to 9 km, constructed with the mainshock focal mechanism (Fig. 9a). Profile of synthetic seismograms for source depths from 6 to 9 km, constructed with the aftershock focal mechanism (Fig. 9b). A moment of 10^{25} dyne-cm was used.

down swing in the radial synthetic is "filled" when the near-field term is included. Synthetics constructed with the aftershock focal mechanism and near-field terms would probably better explain the relative amplitudes of the three components for both earthquakes.

Sensitivity Analysis

The result of a simple structure controlling the waveforms is surprising. Figure 1 indicates that there is considerable geologic complexity along this profile. Ignoring details of faulting and folding, the profile still retains a ridge-basin-ridge structure. Specifically, the energy released during the earthquakes propagated through the San Jose Hills, San Gabriel basin, and the eastern margin of the Verdugo mountains. The second part of this paper investigates sensitivity of the synthetic seismograms to perturbations of the layer over a half-space structure. Smoothed layer boundaries, deep crustal structure, layer thickness, and two-dimensional velocity models were tested. Three-component synthetic seismograms for flat-layered models were computed by the same reflectivity method discussed earlier. The main-shock focal mechanism was used in these synthetics. Synthetic seismograms for the two-dimensional studies were computed with a finite-difference approach (Helmberger and Vidale, 1988). In these analyses, the source depth was kept fixed at 9 km.

Figure 10 shows the results of perturbing the layer over a half-space structure by introducing velocity gradients. All of the perturbed models produce synthetics resembling the layer over a half-space result. This is especially true for Figures 10c and 10d. Velocity gradients are introduced in those models to remove the sharpness of the contact between the two layers. Some of the effects to take note of are the removal of the second multiple (S_2) and the broadening of the Love wave, as compared to Figure 10a. Figure 10b has a linear gradient from the free-surface to the half-space. The shape of the Love wave is severely altered, as are the radial and vertical component synthetics. The second well developed peak on the vertical and radial components is caused by the phase SP, which is a direct S to the free-surface converting to a P wave with a path turning in the linear gradient. This phase becomes more complex when multiple conversions are introduced by more boundaries. Generally it is possible to smooth the contact between the two layers and still obtain synthetics which are good fits to the data; however it is important that there is a well defined surface layer to develop the Love wave and the S_1 multiple. It was found that 1 to 2 km of smoothing of the layer boundary could be tolerated in the synthetics at the frequencies we are modeling.

Figure 11 shows the results of varying deep crustal structure and the effect of the velocity/thickness tradeoff for the shallowest layer. LOHS1 is the preferred model, discussed earlier. Table 1 gives the details of all of the models used in the construction of the following synthetics. Comparison of the synthetics constructed with the LOHS1, SoCal, and LOHS2 models shows that there is some variation, in the waveforms. The SoCal model is an average model of southern California which is used to routinely invert for source location and focal mechanism from first-motion data. The synthetics produced by this model do not fit the data well. The primary reason is the thickness and velocity of the surface layer. This layer is 5 km thick, with a velocity of 3.18 km-s^{-1}. The greatest effect on the tangential components is that the Love wave is not as developed as it is for model LOHS1. For model LOHS2, the surface layer was made thinner and slower. An additional mid-crustal layer was also included. The effects are that the Love wave and the S_2 multiple are more

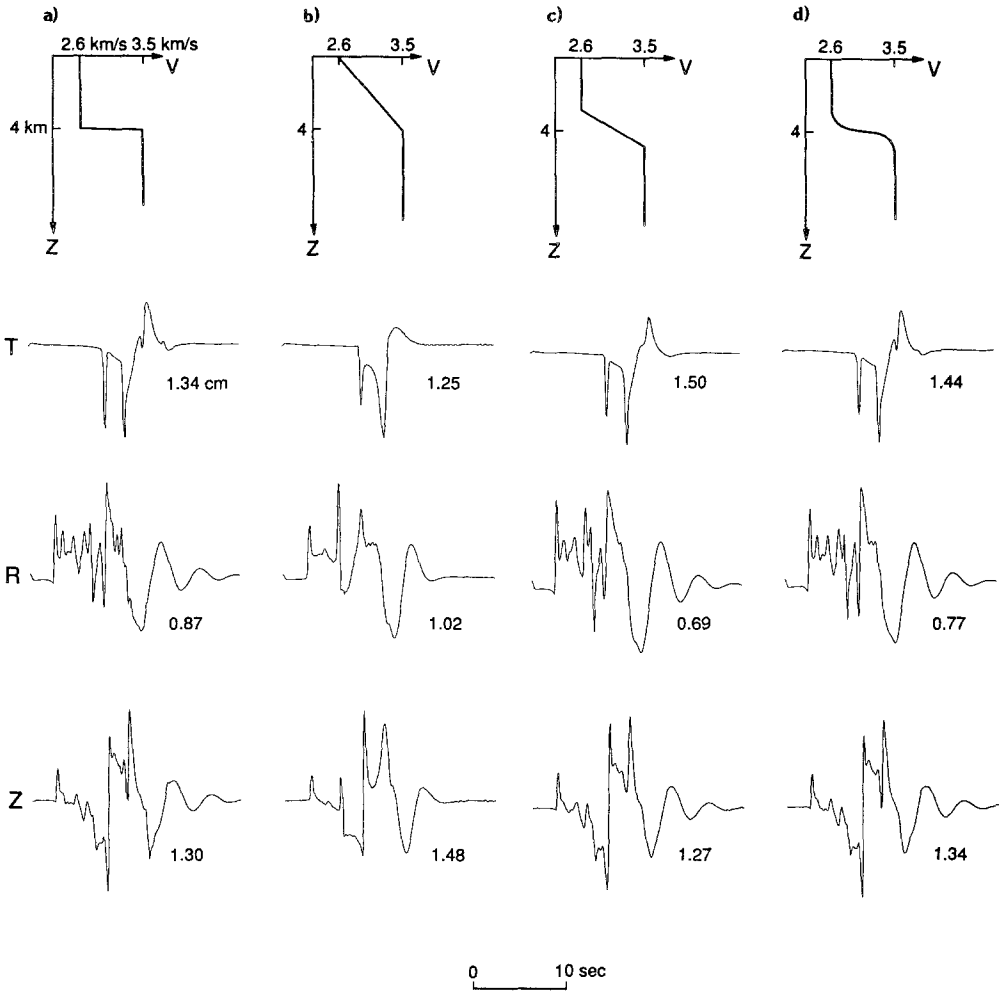

FIG. 10. Boundary sharpness sensitivity assuming a moment of 10^{25} dyne-cm. Each seismogram is scaled to its maximum amplitude. A source depth of 9 km was used.

developed than for model LOHS1. This indicates that the thickness of the surface layer must be less than 5 km and greater than 3 km.

Langston (1989) studied *PS* crustal conversions of teleseismic signals recorded at PAS and obtained a one-dimensional receiver structure for PAS. Model L1 (Table 1) is a modified version of this receiver structure in which the velocity of the surface layer was changed to that of model LOHS1. Model L1 contains a low-velocity zone at depth. Model L2 is the same model as L1 except that the low-velocity zone was removed and replaced with an increasing gradient. Figure 11 shows that the synthetic seismograms do not change very much for these two models as compared to model LOHS1. The details of deep crustal structure are not particularly important in the waveforms of local earthquakes (ranges less than 44 km) for frequencies less than 1 Hz.

Figure 12 shows the results of including lateral variations using a two-dimensional finite-difference calculation. For these models, the two *SH* fundamental faults were computed and convolved with a square-foot singularity to map the line source

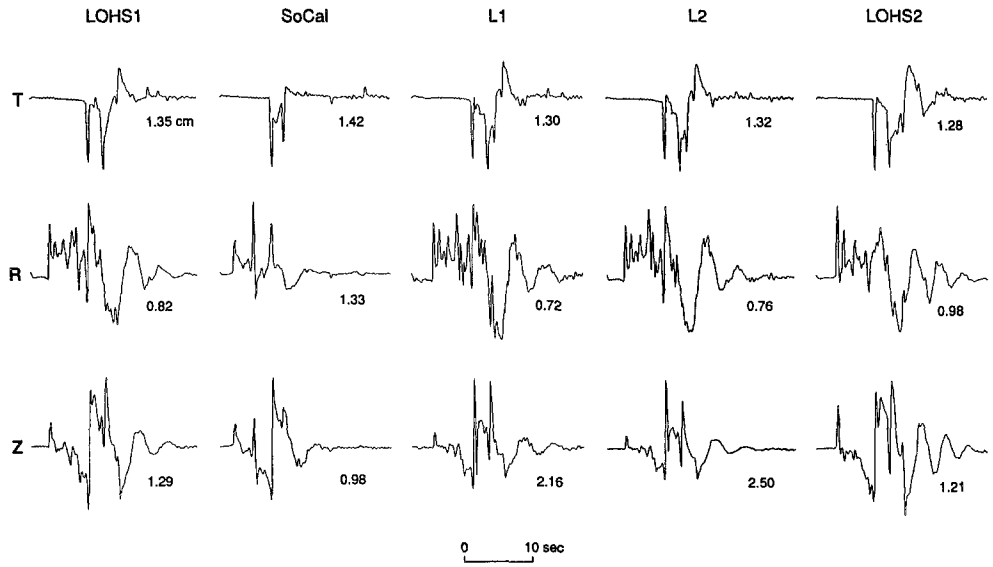

FIG. 11. Flat layered model sensitivity assuming a moment of 10^{25} dyne-cm. Each seismogram is scaled to its maximum amplitude. A source depth of 9 km was used. See Table 1 for the details of the different models used.

response to a point source. The two fundamental faults were summed to produce displacement synthetics with the main-shock focal mechanism. Figure 12a shows the tangential displacement synthetic for a layer over a half-space model. Comparing the reflectivity result (Fig. 10a) with Figure 12a, it is evident that the two methods correlate well. This comparison is useful in identifying the occurrence of artifacts in the finite-difference synthetics. The finite-difference calculation accurately reproduces the result of the reflectivity calculations. However, two artifacts are present. These artifacts arise from reflections from the finite grid boundaries. Since they occur later in time than the Love wave, they do not cause any substantial distortion of the synthetic waveforms.

Figures 12b and c show the effect of a ridge structure introduced beneath the PAS station. The effect is basically a low-pass filter. When an intermediate velocity is introduced into the ridge (Fig. 12c), many of the characteristics of the layer over a half-space are retained, although there is a reduction of the higher frequency energy. The WASP instrument synthetics would be affected by this structure. Since the ridge structure attenuates the upward propagating higher frequency energy, initial downward propagating energy, reflected back to the receiver, would be more important in the WASP synthetics. This figure demonstrates that a ridge structure beneath PAS does not have a large effect at lower frequencies, but may be significant at higher frequencies.

Figures 12d and e show the effect of the addition of a ridge between the source and the receiver. The character of the waveform is completely changed, especially the Love waves. Vidale and Helmberger (1988) found that shear body waves convert to surface waves at the edge of the basin closest to the source and propagate across the basin. Vidale and Helmberger (1988) also saw evidence of surface waves crossing across ridge structures. In our models, the secondary surface waves are typically richer in higher frequencies than those for models with no ridge between the source and receiver (compare Figs. 12a, b, and c to Figures 12 d and e). These higher-

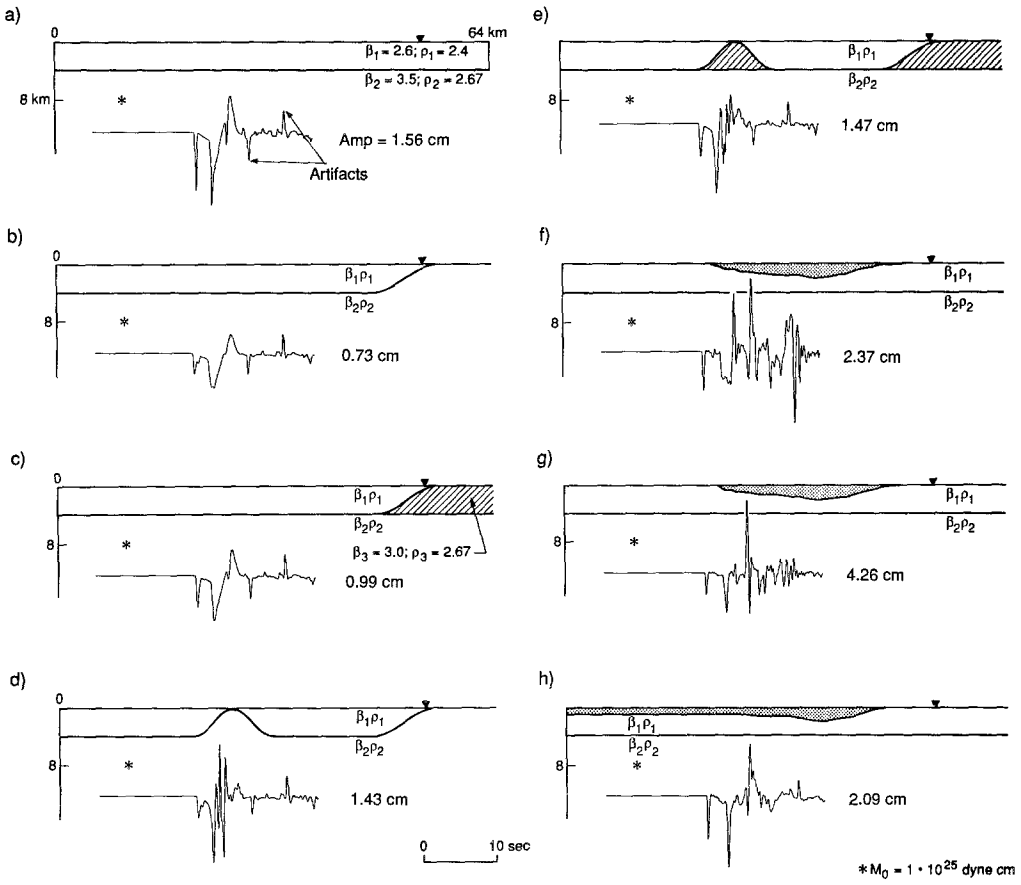

FIG. 12. *SH* finite-difference calculations using ridge structures and realistic basins after Yerkes *et al.* (1965). Dotted region in 12f represents $\rho = 2.0$ g cm^{-3} and $\beta = 1.8$ km s^{-1}. For Figures 12g and 12h, the dotted region represents a linear gradient in velocity with the form $\beta = 1.8 + 0.4z$. The moment used is 10^{25} dyne-cm. Each seismogram is scaled to the maximum amplitude of 12a, except 12f, g, and h. For each synthetic the maximum amplitude is given. A source depth of 9 km was used.

frequency phases are probably critically reflected arrivals generated at the ridge. In fact, the character of the waveform resembles those for shallow sources, within the surface layer (see Fig. 8). The synthetics for these ridge structures do not fit the Upland data. Figures 12f, g, and h explore the possibility of a shallow basin within the surface layer. Figure 12f has a basin with a 1.8 km-s^{-1} shear-wave velocity and a 2.0 gcm^{-3} density. Figures 12g and h differ in that the velocity within the basin is a linear gradient where $\beta = 1.8 + 0.4Z$. The geometry of the shallow basin for Figures 12f and g was interpolated from the depth to basement results of Yerkes *et al.* (1965). In these calculations, the layer at 4-km depth was retained because of its importance in producing the S_1 and S_2 multiple phases as well as the Love wave.

For Figures 12f, g, and h, the synthetics are amplified by 134 per cent to 273 per cent compared to Figure 12a. The durations of the synthetic seismograms are also extended compared to Figures 12a through e. Both of these effects are the result of trapping reverberating energy in the basin which subsequently escapes at the shallow basin boundary. The escaping energy encounters the deeper layer responsible for S_1 and S_2 at near critical angle and is reflected back up to the receiver. The differences in the synthetic waveforms for Figures 12f and g are the result of the

effect of the gradient on the development of a local Love wave within the basin. The basin model lacking a velocity gradient has a slower velocity, which serves to extend the duration of the synthetic waveforms. The addition of a gradient in the shallow sediments also slows down the locally generated Love waves and appears to be a very effective mechanism of producing late arrivals. Figure 12h shows that much of the amplification observed in 12g is due to the energy being trapped by the dipping basin wall near the free surface. Note that shallower sources are more effective at generating surface waves and, thus, at generating stronger coda via this type of scattering. This may be the explanation of the coda arriving in the observed data (for example, see Fig. 7). It appears that case (12c) closely resembles the actual situation at the recording station, where the main effect is to remove the highest frequencies from the flat layer calculation.

Figure 13 shows the radial and vertical component finite-difference synthetics using the model of Figure 12c. These synthetics are compared with the reflectivity calculations for the layer over a half-space. The synthetic waveforms do not change dramatically for this two dimensional structure. The Rayleigh wave seems to be the most affected phase, with a slight phase shift. Array measurements would be required to examine possible timing relationships of higher frequency scattered ridge phases. The results of both the SH and P-SV two-dimensional studies indicate that these structures do not control the shape of the synthetic waveforms, except at higher frequencies, and in the phase of the Rayleigh wave.

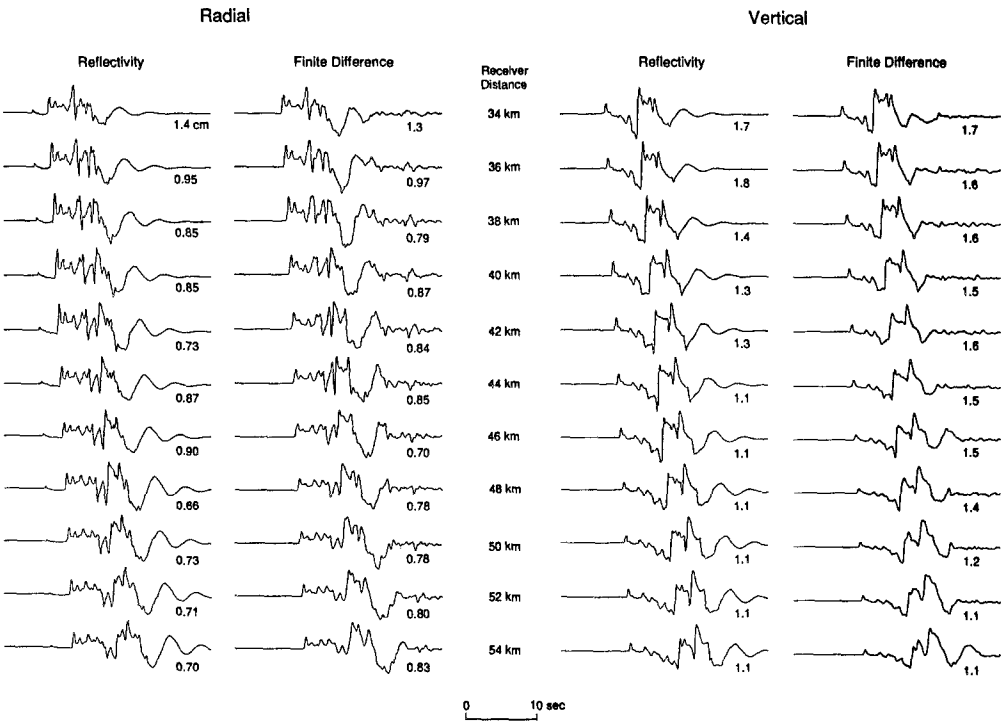

FIG. 13. Radial and vertical component synthetics showing the difference between a flat layer over a half-space (reflectivity synthetics) and the model in Figure 12c (finite-difference synthetics). A moment of 10^{25} dyne-cm is used. Each seismogram is scaled to its maximum amplitude. A source depth of 9 km was used.

Discussion and Conclusions

We envision the usefulness of these Green's functions in several ways. First, they can be used to study less well recorded historic events where the only seismological waveform data available are a pair of long-period horizontal torsion recordings (WALP), as is the case at PAS. This is particularly valuable for studying growth structures in basins (such as Los Angeles basin) under compression, where focal mechanisms are likely to show considerable variation. Second, they can be used to calibrate the empirical Green's function approach in the simulation of large events from small ones (Hartzell, 1978; Mori and Hartzell, 1990; Woods *et al.*, 1990). Mori and Hartzell (1990) use a small aftershock of the same $M_L = 4.6$ Upland event to study the plane of faulting of the main event. Although our objective was to develop Green's functions for this path to PAS and to demonstrate the methodology of studying broadband seismograms to find the Green's functions, it is interesting to compare our results of moment and stress drop estimates with theirs.

The fundamental assumption in the empirical Green's function approach is that the waveform distortions caused by the path and site conditions are shared by the main shock and the aftershock. If the mechanisms are identical, one can use the aftershock P waveforms to generate the main event P waveforms by considering finite rupturing on the two possible focal planes, namely ($\phi = 125°$, $\delta = 85°$, $\lambda = 130°$, or $\phi = 221°$, $\delta = 40°$, $\lambda = 8°$). Mori and Hartzell (1990) find that the southwest-trending plane gave the best results indicating left-lateral motion, which is consistent with the overall motion in the Transverse Ranges frontal fault zone. They obtained a moment estimate of 4.2×10^{22} dyne-cm for the main event from the P-wave amplitude. Their inversion gave a source area of 1 km^2 and a stress drop of 38 bars.

We obtained a larger moment $(6 \pm 2) \times 10^{22}$ dyne-cm by modeling the amplitudes of the three-component displacement data convolved with a Press-Ewing instrument response. A considerably larger stress drop, based on the far-field time duration, τ, was estimated, by assuming that:

$$\tau = \frac{a}{\beta}\left[\frac{16}{7\pi} + \left(\frac{1}{0.8} + \sin\,\delta\right)\right]$$

where a is the fault dimension (circular fault), β is the shear velocity, and δ is the angle between the normal to the fault plane and the ray path (Cohn *et al.*, 1982). The trapezoidal far-field time function discussed earlier, can be represented by a triangular time function (Helmberger and Malone, 1975), where $\tau = 0.5\delta T_1 + \delta T_2 + 0.5\delta T_3$. For a τ of 0.3 sec, this expression yields an estimate of fault dimension a, of 0.4 km. Assuming, $\delta\sigma = 7M_o/16a^3$ (Kanamori and Anderson, 1975), where $\delta\sigma$ is stress drop and M_o is moment, and a as defined above, a stress drop of 410 bars is obtained. This estimate of stress drop is considerably larger than Mori and Hartzell's (1990) estimate. However, different models of fault rupture were used. Recall that in this study the same source-time function was used for both the main shock and the aftershock. The moment of the main shock was found to be about six times larger than that of the aftershock, and therefore the stress drop of the main shock should be larger relative to the aftershock. Mori and Hartzell (1990) report that rupture on the southwest-trending fault plane (their preferred fault plane) propagated upward and to the southwest toward PAS. Correcting for

unilateral rupture toward PAS would increase our estimate of fault dimension and would result in a lower estimate of stress drop. In any case, clearly a combination of numerical and empirical approaches would be the most powerful, in which the longer-period properties, namely moment, effective time history and orientation, are modeled numerically, and shorter-period effects, namely rupture properties, are modeled empirically. A discussion of the implications of using the same source–time function for both events follows.

The same source–time function for both the main shock and the aftershock was used in calculating our synthetics and Q was neglected. Since Q trades off with far-field source–time-function width, it has been indirectly accounted for. Therefore the time function used in this paper is a composite of the far-field time function and a Q operator. If Q was included in the synthetics presented in this paper, the effect would be a reduction in amplitude and high-frequency content. The effect would be similar to that shown in Figure 12c. At 44 km there would be little change of the overall synthetic waveforms. Thus we are not able to obtain a good estimate of Q with just the data used in this study. To constrain the effect of Q, a determination of the source–time function close to the source would be needed. Then, in comparing the near-field and far-field source–time functions, the effect of Q could be evaluated. In addition, we have demonstrated that some complicated receiver structures can behave in a manner similar to Q. This shows that care must be used in differentiating the Q effect from receiver structure.

The aftershock is also richer in higher frequencies than the main shock, suggesting a shorter source–time function for this event. If we assume the stress drop of the aftershock to be that of the main shock (410 bars), then a τ of 0.16 sec is obtained. The synthetic seismograms are not significantly improved using this time function. Our model may be too simple to explain the higher frequencies or perhaps, there is a higher level of high frequency noise on the aftershock record. In any case, the use of Q or a shorter source–time function would serve to increase our estimate of stress drop.

In conclusion, it is possible to interpret local broadband records with relatively simple models. The broadband records facilitate the identification of different arrivals, particularly phases with different frequency content (i.e., near-field, post-critical, and surface-wave phases). The results of the forward modeling indicate that the waveforms of the two Upland, California, earthquakes are controlled by the relatively slow material at the surface for which a single-layer structure is an adequate approximation. The forward modeling approach used here is also useful in studying source complexities. This is facilitated by studying two or more earthquakes in a given area. The differences in the waveforms can be understood in terms of differing focal mechanism, location, source–time function, or in dislocation complexities. In the case of the $M_L = 4.6$ Upland, California, earthquake, it was found that the waveforms were better modeled with synthetics computed with a source depth of 6 km, roughly 3 km shallower than the array location. This is not surprising in that a strong trade-off in depth versus origin time exists in earthquake location solutions. Thus, one of the first contributions of local broadband waveform data will be on source depth control.

The sensitivity analyses indicate that the layer must be between 3- to 5-km thick, but the boundary of the layer can be smoothed with a 1- to 2-km-wide velocity gradient. Deeper crustal structure is not important at this distance for frequencies less than 1 Hz. Two dimensional near receiver ridge structures attenuate the higher frequencies (>1 Hz.). Neither of the closed basin models nor the shallow basin

models satisfied the data. However, the extended duration produced by shallow basins may account for the observed extended duration of S-wave packets for other earthquakes which occur south of Upland (Figs. 1 and 2). Fortunately, the relative insensitivity of the synthetics to details of boundary sharpness, layer thickness, and to some degree two-dimensional near receiver structure, shows that useful Green's functions can be found without knowing the fine structural details.

ACKNOWLEDGMENTS

The authors would like to acknowledge Mrinal Sen and Richard Stead for their help with the computer codes. We would like to thank Brad Woods, David Wald, and Lorraine Hwang for their meaningful reviews. We especially thank Hiroo Kanamori for his review and efforts in setting-up the Streckeisen instrument. We also thank J. Vidale for his review and suggestions and S. Grand for suggesting that we include Figures 8 and 9 in our discussion of depth dependence. This research was supported by the Advanced Research Projects Agency of the Department of Defense and was monitored by the Air Force Geophysics Laboratory under the contract F1962889K0028. Contribution No. 4838, Division of Geological and Planetary Sciences, California Institute of Technology, Pasadena, California.

REFERENCES

Cohn, S. N., T. Hong, and D. V. Helmberger (1982). The Oroville earthquakes: a study of source characteristics and site effects, *J. Geophys. Res.* **87,** 4585–4594.

Hartzell, S. (1978). Earthquake aftershocks as Green's functions, *Geophys. Res. Lett.* **5,** 1–5.

Helmberger, D. V. (1974). Generalized ray theory for shear dislocations, *Bull. Seism. Soc. Am.* **64,** 45–64.

Helmberger, D. V. (1983). Theory and application of synthetic seismograms, in *Earthquakes: Observation Theory and Interpretation*, H. Kanamori (Editor), Soc. Italiana di Fisica, Bologna, Italy, pp 174–222.

Helmberger, D. V. and S. D. Malone (1975). Modeling local earthquakes as shear dislocations in a layered half space, *J. Geophys. Res.* **80,** 4881–4888.

dimensional numerical codes, *Bull. Seism. Soc. Am.* **78,** 109–121.

Kanamori, H. and D. L. Anderson (1975). Theoretical basis of some empirical relations in seismology, *Bull. Seism. Soc. Am.* **65,** 1073–1095.

Langston, C. (1989). Scattering under Pasadena, California, *J. Geophys. Res.* **94,** 1935–1952.

Mori, J. and S. Hartzell (1990). Source inversion of the 1988 Upland earthquake: determination of a fault plane for a small event, *Bull. Seism. Soc. Am.* **80,** 507–518.

Vidale, J. E. and D. V. Helmberger (1988). Elastic finite-difference modeling of the 1971 San Fernando, California, earthquake, *Bull. Seism. Soc. Am.* **78,** 122–141.

Woods, B. B., L. Zhao, D. V. Helmberger, H. Thio, and H. Kanamori (1990). The Loma Prieta Earthquake Sequence as Observed at Pasadena (submitted for publication).

Yerkes, R. F., T. H. McCulloh, J. E. Schoellhamer, and J. G. Vedder (1965). *Geology of the Los Angeles Basin California: An Introduction, U.S. Geol. Surv. Profess. Pap. 420-A.*

SEISMOLOGICAL LABORATORY
CALIFORNIA INSTITUTE OF TECHNOLOGY
PASADENA, CALIFORNIA 91125

Manuscript received 20 February 1990